PCCP

PAPER

View Article Online
View Journal | View Issue

Cite this: *Phys. Chem. Chem. Phys.*, 2019, **21**, 10594

Determination of element–deuterium bond lengths in Zintl phase deuterides by ^{2}H-NMR†

Robin Guehne,[ab] Henry Auer,*[c] Holger Kohlmann,[c] Jürgen Haase[a] and Marko Bertmer*[a]

Received 16th January 2019,
Accepted 3rd May 2019

DOI: 10.1039/c9cp00292h

rsc.li/pccp

The Zintl phase deuterides $CaSiD_{4/3}$, $SrSiD_{5/3}$, $BaSiD_2$, $SrGeD_{4/3}$, $BaGeD_{5/3}$ and $BaSnD_{4/3}$ were investigated by nuclear magnetic resonance (NMR) spectroscopy and density functional theory (DFT) calculations to reliably determine element–deuterium bond lengths. These compounds show deuterium bound to the polyanion and deuteride ions in tetrahedral cationic voids. With ^{2}H-NMR experiments we characterised the individual signals of the two distinct crystal sites. Quadrupolar coupling constants (C_Q) of the anion-binding site were determined as 58 to 78 kHz (Si compounds), 51 to 61 kHz (Ge compounds) and 38 kHz (Sn compound). These values agree well with the quadrupole couplings derived from DFT using optimized structural models. We further calculated the general element–deuterium distance dependency of C_Q using DFT methods that allow an accurate determination of bond lengths *via* the ^{2}H quadrupole interaction. The thus determined bond lengths are evaluated as d(Si–D) = 1.53–1.59 Å, d(Ge–D) = 1.61–1.65 Å and d(Sn–D) = 1.86 Å. Chemical shifts of the anion-binding site range from 0.3 to 1.3 ppm. The isotropic chemical shifts of the tetrahedral sites are 5.1 ppm ($CaSiD_{4/3}$), 7.0 to 10.0 ppm (Sr compounds) and 10.7 to 11.6 ppm (Ba compounds).

1 Introduction

Zintl phases are polyanionic compounds. They consist of an electropositive metal from the s-block (or a rare earth metal) and a more electronegative element from group 13 to 16. The compounds can be formally described by an ionic picture. The anions do not reach an electron octet thus forming covalent element–element bonds according to the general 8-N rule.[1–4]

Zintl phase hydrides can be described by the same formalism. Hydrogen shows a similar or even higher electronegativity than the p-block element. It can be incorporated in two ways: (i) hydrogen can form an anion (H^-) that is exclusively coordinated by cations (interstitial hydride), or (ii) it can form a heteropolar bond towards the polyanion ($H^{\delta-}$, formally H^0, polyanionic hydride).[5]

There are several examples of group 13 polyanionic hydrides. For example, $SrAlH_2$,[6] $AeGaH_2$,[7] and $AeTrTtH$[8–11] (*Ae* = Ca, Sr, Ba, *Tr* = Al, Ga, In, *Tt* = Si, Ge, Sn) show puckered, honey-comb like six-rings of Tt^- and $(TrH)^-$ anions. According to inelastic neutron scattering and quantum chemical calculations these compounds show a covalent *Tr*–hydrogen interaction.[10–13] Further examples are polyethylene-like $(GaH_2)^-$,[14,15] propane-like $(Ga_3H_8)^{3-}$,[16] or neo-pentane-like $Ga(Ga_4H_{12})^{5-}$ [14] polyanions. In contrast the polyanions in $NdGaH_{1.66}$ and $GdGaH_{1.66}$ show only a weak element–hydrogen interaction according to diffraction-derived bond lengths and calculations.[17–19]

The situation for group 14 polyanionic hydrides is still ambiguous. There are contradictory works on $CaSiH_y$ ($1.0 < y < 1.33$) claiming a covalent bond (d(Si–H) = 1.58 Å)[20] or only a weak interaction (d(Si–H) = 1.84 Å).[21] Recently, some of us determined the crystal structures of the homologue systems $BaSiH_{1.9}$, $SrGeH_{1.2}$ and $BaSnH_{1.3}$[22] as well as $SrSiH_{1.5}$ and $BaGeH_{1.6}$.[23,24] The compounds exhibit hydride anions in tetrahedral cationic voids and additional hydrogen binding to the polyanion. Due to short bond lengths, there is strong indication for a covalent interaction, but the estimated uncertainties of a Rietveld based analysis are rather high. This work investigates deuterated samples of Zintl phase hydrides. We apply ^{2}H nuclear magnetic resonance (NMR) and interpret the results based also on density functional theory (DFT) calculations, to improve the bonding picture.

In ^{2}H NMR, the electric quadrupole interaction is a very sensitive probe for the local distribution of charges surrounding the nucleus.[25] The quadrupole coupling constant, $C_Q = e^2qQ/h$ sets the peak distance, Δ (in frequency units), observed in the powder spectra for this $I = 1$ nucleus for uniaxial symmetry ($\eta = 0$) of the quadrupole tensor, as expected from a covalent bond, *i.e.*,

$$C_Q = \frac{4}{3}\Delta. \quad (1)$$

[a] *Felix Bloch Institute, Leipzig University, Linnéstrasse 5, 04103 Leipzig, Germany. E-mail: bertmer@physik.uni-leipzig.de*
[b] *MacDiarmid Institute, School of Chemical and Physical Sciences, Victoria University of Wellington, P.O. Box 600, Wellington 6140, New Zealand*
[c] *Department of Inorganic Chemistry, Leipzig University, 04103 Leipzig, Germany. E-mail: henry.auer@uni-leipzig.de*

† Electronic supplementary information (ESI) available. See DOI: 10.1039/c9cp00292h

As usual, eQ is the known electric quadrupole moment of ^{2}H and h denotes the reduced Planck's constant, while $eq = V_{ZZ}$ (and $\eta = 0$) defines the symmetric electric field gradient (EFG) at the nucleus' site that was calculated with DFT.

Based on our measurements we determine group 14 element–deuterium bond lengths with substantially improved accuracy through a combination of experimentally determined quadrupole interactions and density functional theory (DFT) calculations. We further develop a more comprehensive picture of the NMR of Zintl phase deuterides and its relation to their general chemistry.

2 Experimental

2.1 Synthesis

All manipulations were done in an argon filled glove box. Moisture and oxygen content were kept below 1 ppm each. The Zintl phases were prepared by stoichiometric mixtures of the respective elements using tantalum metal jackets which were subsequently sealed and placed in fused silica ampoules at reduced pressure. The deuterides were prepared in a Nicrofer 5219Nb-alloy 718 autoclave at typical D_2 gas pressures of 5 to 9 MPa and 473 K. Details are given elsewhere ($SrSiD_{5/3}$ and $BaGeD_{5/3}$;[23,24] $BaSiD_2$, $SrGeD_{4/3}$ and $BaSnD_{4/3}$[22]).

The Zintl phase CaSi was prepared from the elements as well (Si: abcr, 99.9999%; Ca: Alfa Aesar, 99.5%). The reactants were placed in tantalum jackets which were sealed and put into fused silica ampoules under reduced argon pressure. The samples were heated with 2.2 K min^{-1} to 1573 K and kept there for one hour. CaSi was annealed at 1473 K for 12 h. In the literature CaSi typically is fast quenched in cold water.[26,27] We want to emphasize that this step is crucial to obtain samples reactive towards hydrogen. $CaSiD_{4/3}$ was prepared in an autoclave reaction of CaSi under 15 MPa D_2 pressure at 523 K for 72 h. The sample was annealed for 72 h.

2.2 Nuclear magnetic resonance

NMR measurements have been carried out on powders sealed in evacuated quartz tubes. Magic angle spinning (MAS) experiments were carried out using MAS zirconia rotors equipped with airtight caps. External static magnetic fields of 9.4 T, 11.7 T, and 17.6 T in combination with Bruker (Bruker Corporation, Billerica, MA, USA) spectrometers (AVANCE 400/750 and AVANCE III HD) were used. Homebuilt static and 4 mm Bruker MAS probes were employed. Spectra were recorded with free induction decay (FID – static and MAS) and solid-echo ($\pi/2$–τ–$\pi/2$) pulse sequences[28,29] (only static) with typical $\pi/2$-pulse lengths of 3 to 5 μs and pulse separation times τ = 30 μs. Recycle delays were set to 500 s due to spin lattice relaxation times (T_1) of 50 to 100 s depending on sample, crystal site and external magnetic field.

Low MAS spinning frequencies were used to generate sufficiently detailed spectra that allow accurate fitting of the quadrupolar lineshapes. For isolating isotropic signals, higher spinning frequencies up to 8 kHz were used. Data analysis was done with *Bruker Topspin*, *dmfit*,[30] and *OriginPro 7.5G* software package (OriginLab Corporation, Northampton, MA, USA). Deuterated Water (D_2O) was used for optimizing measurement conditions and referencing.

2.3 Density functional theory (DFT) calculations

The *Abinit* package[31–35] was used to calculate quadrupole splittings. Calculations were performed using the generalized gradient approximation (GGA) as implemented in the Perdew–Burke–Ernzerhof (PBE) functional.[36,37] Projector-augmented wave (PAW)[38,39] atomic data were taken from the *JTH PAW atomic dataset table*.[40,41] Electron densities and, therefore, the EFGs at the corresponding deuterium sites were calculated with a SCF threshold of 10^{-9} Hartree regarding total energy (toldfe) on a $4 \times 12 \times 12$ (*Pnma*-$BaSiH_2$), $4 \times 12 \times 4$ (*Pnma*-$CaSiH_{4/3}$, -$SrGeH_{4/3}$, -$BaSnH_{4/3}$) or $4 \times 12 \times 2$ (*Pnma*-$SrSiH_{5/3}$, -$BaGeH_{5/3}$) Monkhorst–Pack[42] k-point grid which corresponds to about 0.01 Bohr^{-1} k-point accuracy. For molecular calculations SiH_4, GeH_4 and SnH_4 were placed in a large box (a = 20 Å) with Γ as a single k-point. Since previous density of states (DOS) calculations showed no or just pseudo band gaps, the systems were treated metallic with 0.001 Hartree Gaussian smearing. This value was tested for chemically similar systems and seemed appropriate. The kinetic energy cut-off (ecut) was set to 25 Hartree which is the suggested high value for hydrogen. The corresponding pawecutdg was set to 2·ecut. The convergence of C_Q was tested with regard to ecut in detail for the systems SiH_4, GeH_4 and $BaSiH_2$. Convergence regarding the k-grid was tested in detail for $BaSiH_2$. The used values show an agreement better than 0.25 kHz in C_Q. For deuterium an electric quadrupole moment of 2.86×10^{-3} barn[43,44] was used.

3 Results

As the structural properties of the materials under consideration are crucial for the interpretation of their NMR results, we will first review the crystallographic details that are published already elsewhere.[20–24]

Within the homologue series of the Zintl phase deuterides $AeTtD_{(1+y)}$, Ae = Ca–Ba, Tt = Si–Sn, three distinct structure types occur (Fig. 1). All structure types show one deuterium atom per formula unit in pseudo-tetrahedral Ae_4 voids (interstitial hydride). The remaining deuterium atoms bind to Tt atoms (polyanionic hydride). According to the Zintl concept, the compounds can be formulated as $(Ae^{2+}\ D^-)(Tt^-)_{1-y}(TtD^-)_y$. Therefore, the Tt atoms can be expected to be three-binding. This is realized by the formation of Tt zigzag chains in crystallographic b direction (2 bonds). The remaining bond is saturated by deuterium ($BaSiD_2$ structure type) or by an additional connection of the chains in crystallographic c direction. The $CaSiD_{4/3}$ structure type is formed by a deuterium termination after three of these chains. The $SrSiD_{5/3}$ structure type shows two different polyanions. One is a Tt chain where each atom is saturated by deuterium as found for $BaSiD_2$. The other one exhibits an additional Tt–Tt bond connecting two chains. The remaining Tt atoms are bound to deuterium. Furthermore, diffraction showed that the chain-coordinating deuterium site is always under-occupied

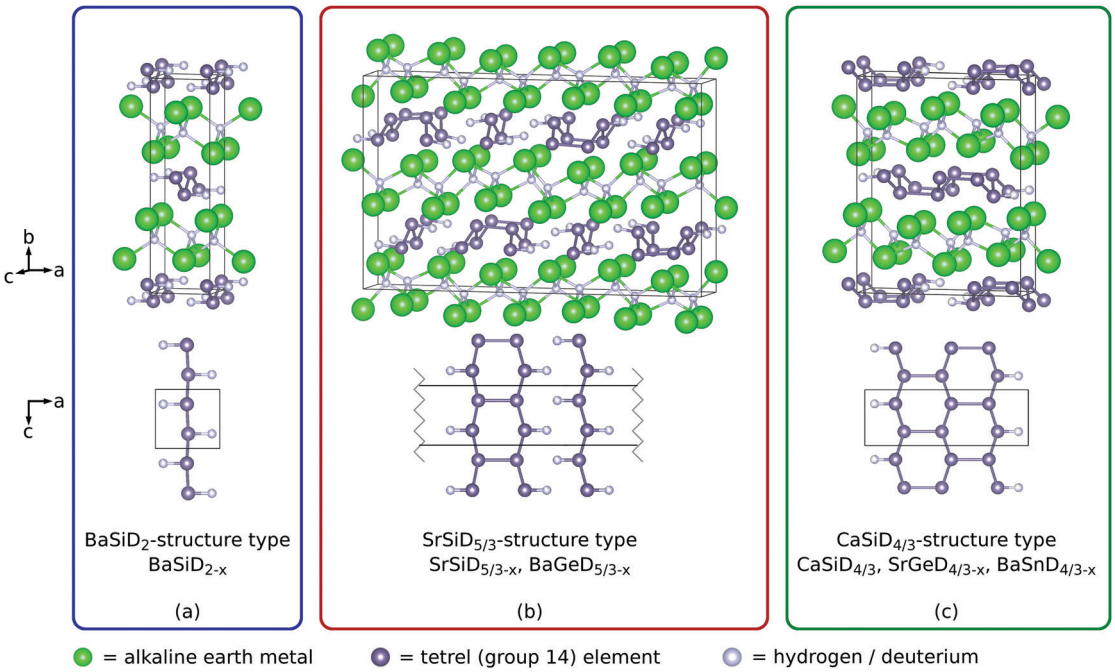

Fig. 1 The three structure types (space-group type *Pnma* for all of them) adopted by the Zintl phase deuterides under investigation and a projection of the polyanions.

(details were given elsewhere[22–24]) which is indicated by a correction term x in the chemical formula. The compounds $CaSiD_{4/3-x}$,[20,21] $SrGeD_{4/3-x}$[22] and $BaSnD_{4/3-x}$[22] crystallize in the $CaSiD_{4/3}$ type. $SrSiD_{5/3-x}$[23,24] and $BaGeD_{5/3-x}$[23,24] adopt the $SrSiD_{5/3}$ structure type. The compound $BaSiD_{2-x}$[22] shows its own structure type ($BaSiD_2$ type).

3.1 NMR

From the ^{2}H NMR spectra, we determined quadrupole coupling constants (C_Qs), isotropic shifts, linewidths and estimated the relative intensity of resonances in the present samples. The corresponding static spectra are given in Fig. 2, with more NMR parameters listed in Table 1.

The quadrupole splitting constant C_Q is directly accessible *via* the distance of the horns of the axial symmetric quadrupole powder patterns (or peaks in Fig. 2), see eqn (1). The results were confirmed by fitting slow MAS spectra. Field dependent measurements were used to separate contributions from field dependent (shift anisotropy) and field independent (quadrupole and dipole interactions) effects. It was found that both lines, the narrow as well as the quadrupole split one, are essentially magnetic field independent.

The NMR spectrum of each compound is composed of a narrow resonance line in the middle of a broad quadrupole powder pattern that becomes visible through the two horns of the quadrupole doublet. We carefully examined the spectra of static as well as MAS experiments and found no evidence for a deviation from axial symmetry, *i.e.* $\eta = 0$. Note that there is no central transition in quadrupolar split deuterium spectra (contrary to half-integer spin systems under quadrupole interaction). As expected, in MAS spectra, the broad quadrupole pattern is broken up into a manifold of spinning sidebands (data shown in ESI†). The reduced linewidths of the MAS spectra also reveal a shift difference between the narrow and the broad resonances (see below).

These two signals, different in shape and shift, represent very different local environments of the related nuclei, in agreement with the crystal structures as described above. On the basis of the general similarities of the crystal structures investigated within this work, *i.e.* a high symmetry environment (cubic pseudo-symmetry) and a low symmetry environment (no pseudo-symmetry) for D atoms,[23,24] we find consistently with our report on $BaSiD_{2-x}$ and $SrGeD_{4/3-x}$,[22] that the narrow resonance lines in Fig. 2 can be assigned to ^{2}H nuclei residing in the Ae_4 voids (high symmetry), whereas the quadrupolar split ones belong to *Tt* chain sites (low symmetry). Measured shifts confirm this assignment which is further substantiated through the relative intensity of both lines reproducing in good approximation the relative occupation of both crystal sites. The quadrupole splitting being consistently axially symmetric for each sample reflects the cylinder symmetry of the chemical bond that gives rise to the EFG at the nucleus' site.

In $BaSiD_{2-x}$ with its separated, unconnected chains, there is one crystallographic site of deuterium binding to the Si-chain and another located within the Ba_4 voids. This structure allows the maximum amount of hydrogen/deuterium to be brought into the system, *i.e.* $AeTtD_2$. Consistently, we identify a well defined signal for each crystal site (*cf.* Table 1) of comparable intensity.

In the $CaSiD_{4/3-x}$ structure type three chains are interconnected. These systems also exhibit only one crystallographic deuterium site saturating the non-connected *Tt* atoms, however, there are three crystallographic deuterium sites within Ae_4 voids which

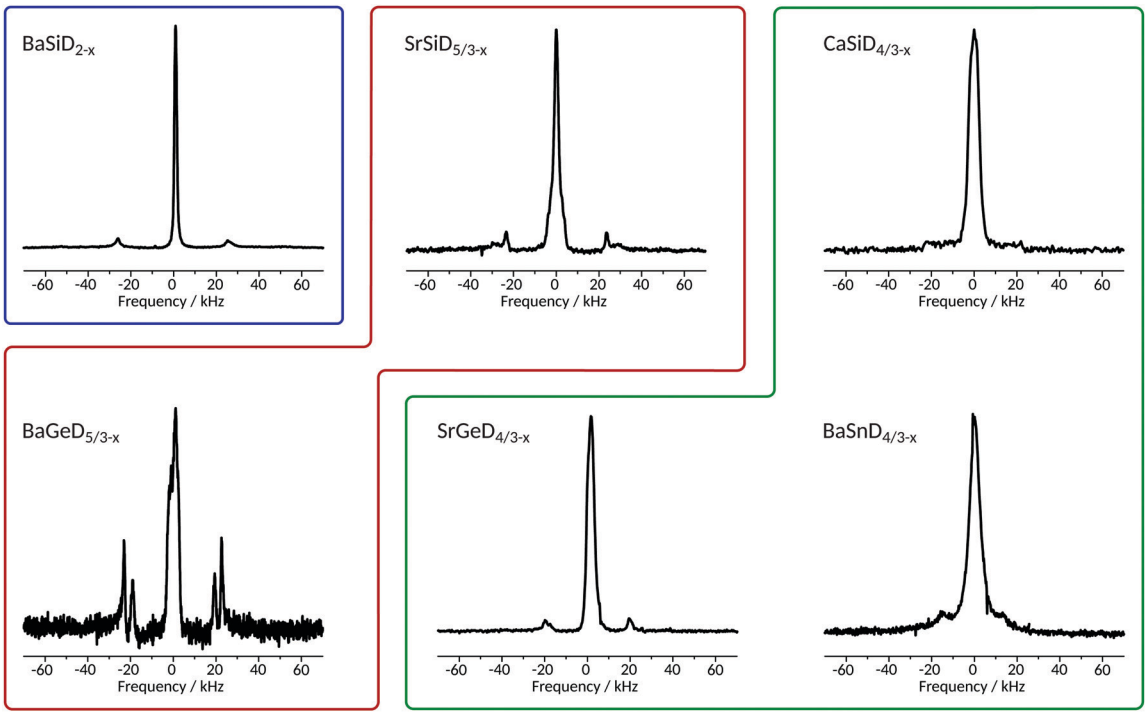

Fig. 2 Static ^{2}H spectra of Zintl family deuterides obtained at a magnetic field of 17.6 T (except for $CaSiD_{4/3-x}$ obtained at 11.7 T) with a $\pi/2$-pulse length of 5.7 μs (3 μs for $CaSiD_{4/3-x}$) averaging between 144 and 304 scans (depending on sample). Each spectrum consists of a narrow central line and a broad, quadrupolar split one. The quadrupole interaction can be evaluated by the distance in frequency units of the two horns which is directly related to C_Q as defined in the introduction. Coloured frames correspond to isotypic structures as indicated in Fig. 1.

Table 1 Comparison of experimental and DFT (optimized structural models) calculated NMR parameters. C_Qs and static linewidths (Λ) are given in kHz, isotropic shifts in ppm. Experimentally, the quadrupole asymmetry parameter η is assumed to be equal to 0. In case of $C_{Q,DFT}^{void}$ and η_{DFT}^{void} the full range of values as derived from DFT is presented. Note, negative values for C_Q will not change a corresponding NMR spectrum due to symmetry. In case of $SrGeD_{4/3-x}$, the narrow line in Fig. 2 appears to be superimposed by a narrow and a much broader line. We therefore give two approximated widths of two lines. The deviation from the ideal composition ($x_{neutron}$) is taken from the literature[22–24]

Compound	$x_{neutron}$	$C_{Q,exp}^{chain}$	$C_{Q,DFT}^{chain}$	η_{DFT}^{chain}	Shift^{chain}	Λ^{void}	$C_{Q,DFT}^{void}$	η_{DFT}^{void}	Shift^{void}
$BaSiD_{2-x}$	0.13(2)	69(1)	65.3	0.06	1.0	1.6(1)	0.81	0.87	10.7
$SrSiD_{5/3-x}$	0.17(2)	63(1)/78(3)	57.7/63.5	0.02/0.11	1.4	1.9(1)/7.2(2)	0.95–(−7.14)	0.14–0.64	7.0
$CaSiD_{4/3-x}$	0.03–0.13	58(2)	57.6	0.01	0.3	5.4(2)	3.92–8.36	0.24–0.32	5.1
$SrGeD_{4/3-x}$	0.139(3)	52(2)	47.7	0.02	0.5	3.9(3)	2.3–(−5.9)	0.03-0.64	10.0
$BaGeD_{5/3-x}$	0.10(3)	51(2)/61(2)	50.1/55.5	0.02/0.04	1.3	5.7(5)	0.31–(−4.31)	0.4–0.86	11.6
$BaSnD_{4/3-x}$	0.055(2)	38(2)	36.9	0.02	0.7	5.1(3)	−1.3–(−7.06)	0.41–0.89	11.2

are no longer as regular as found for $BaSiD_{2-x}$. The maximum number of H/D atoms is necessarily reduced, *i.e.* $AeTtD_{4/3}$. NMR spectra consist of a quadrupole split resonance and a narrow line in the middle. The relative intensity of the former resonance is significantly reduced compared to the latter one, a result much different to what is found in the case of $BaSiD_{2-x}$. This reflects the altered relative occupation due to larger polyanions.

The $SrSiD_{5/3-x}$ structure type, realized in $SrSiD_{5/3-x}$ and $BaGeD_{5/3-x}$, is crystallographically the richest case in the present study (Fig. 1). Single chains as in $BaSiD_{2-x}$ alternate in *c* direction with a deuterium saturated double row (two connected chains). There are four crystallographically independent chain-binding deuterium sites present (D1 to D4; see Fig. 5), two for each polyanion. Due to molecular pseudo-symmetry there are only two quadrupole couplings that differ in C_Q and η. For deuterium ions within Ae_4 voids, six crystallographic sites can be identified. Hence, these voids are even more irregular than in the $CaSiD_{4/3-x}$ case. For the two samples we do in fact find two different quadrupole splittings of comparable intensity (Fig. 2) and a substantially broadened resonance in the center.

3.2 DFT calculations

3.2.1 DFT optimized structural models. The quadrupole coupling constants (C_Qs) were calculated using DFT optimized structures as given in the literature.[20,22–24] These models assume a full occupation of all deuterium sites, *i.e.* neglecting the non-stoichiometry term *x*. The DFT models agree well with the heavy element (*i.e.*, non-hydrogen atom) partial structure as determined by X-ray and neutron diffraction. Deuterium positions within tetrahedral voids are also equally described by experiment

and theoretical modelling. Neutron diffraction derived data for the tetrel binding deuterium sites suffer from large estimated uncertainties (e.u.) up to 0.05 Å. Due to the low precision of the bond lengths determined by Rietveld refinement, this leads to a large spread of the nominal *Tt*–D distances. DFT derived models give a narrower distribution for the different bonds and systems which is mostly still within 3 e.u. of the experimental data.

As shown below, C_Q values only depend on the *Tt*–D distances. Thus, we constrain our discussion to the DFT optimised models here.

DFT calculations of the optimized structural models clearly show that deuterium in Ae_4 voids exhibit a very small EFG ($C_Q < 9$ kHz), while for the *Tt* coordinating sites a considerable EFG ($C_Q > 35$ kHz) is present. The tetrahedral voids are a pseudo-cubic environment for deuterium. Still, crystallographic symmetry (point symmetry *m*) is lower and the asymmetry parameter η deviates from zero considerably (Table 1). The deuterium atoms at the *Tt* chains are also located on a low symmetric site (point symmetry *m*). They show vanishing asymmetry parameters smaller than 0.1 (in most cases even $\eta < 0.04$; Table 1) indicating almost perfect axial symmetry. The direction of the main component of the EFG deviates less than 5° from the symmetry axis of the bond which is the connecting line of the atoms. The quadrupole splittings of the *Tt*-binding site can be compared to the experimental values. The C_Q values agree very well (Table 1).

3.2.2 Modelling distance dependency. The distance dependence of the quadrupole interaction C_Q was determined by DFT calculations. The *Tt*–D bond length of the Zintl phase deuterides $CaSiD_{4/3}$, $BaSiD_2$ and $SrGeD_{4/3}$ was varied systematically. All atomic positions as well as unit cell size were kept fix. These parameters are reliably determined by diffraction experiments. The DFT models represent these experimental values well. The deuterium atoms binding to *Tt* were moved in direction of the bond without changing the angle. For comparison the distance dependency of C_Q was calculated for the molecular compounds SiD_4, GeD_4 and SnD_4. They are well suited as model compounds since (i) the quadrupole interaction exhibits pure axial symmetry, and (ii) the bonding is covalent. Additionally, there are experimental bond lengths and C_Q values available from the literature (see below). The results are shown in Fig. 3 (Si–D bonds) and Fig. 4 (Ge–D bonds). The C_Q-distance dependency of a Sn–D bond was only calculated for the molecular model compound SnD_4 and is given in the ESI† (Fig. S4).

The distance dependency of C_Q regarding the *Tt*–D bond length for covalent, molecular deuterides and the Zintl phase deuterides agree well, suggesting similar electronic structures, *i.e.*, a covalent character of the *Tt*–D bond. Furthermore, while the surrounding of a given polyanionic deuteride seems not to affect the quadrupolar interaction considerably, effects on the asymmetry parameter η are small as well. It starts to increase significantly for *Tt*–D distances much larger than expected for the $AeTtD_y$ systems, *i.e.* larger than 1.80 Å (Si and Ge compounds). The dependency of C_Q and η in regard to the dihedral angle of deuterium towards the plane of the zigzag chain was evaluated for $BaSiD_2$ (see ESI,† Fig. S1). There is hardly an effect on the magnitude of the quadrupolar interaction (less than 5 kHz for ±10°). Decreasing the dihedral angle increases C_Q, while increasing the angle strongly affects the asymmetry parameter. Bond angles smaller than 90° are unlikely due to chemical reasoning in agreement with experimental results where no evidence for an asymmetric quadrupole interaction could be found.

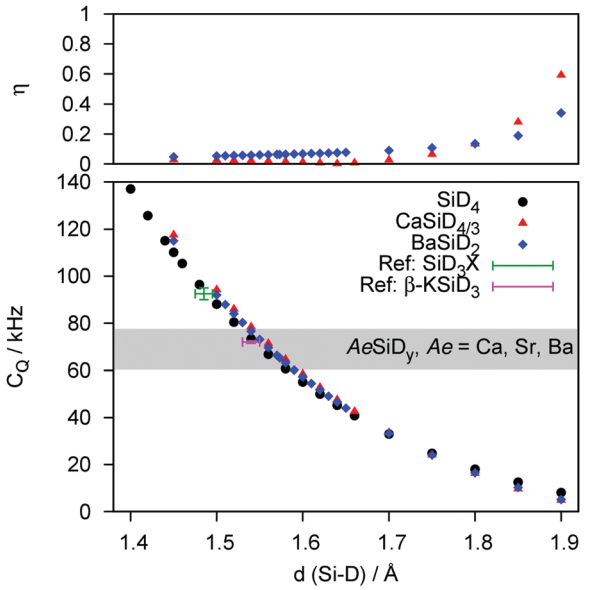

Fig. 3 DFT derived distance dependence of C_Q and the corresponding asymmetry parameter η of SiD_4, $CaSiD_{4/3}$, and $BaSiD_2$. Experimental data of silane derivatives SiD_3X (X = D, CH_3, C_5H_6) and β-$KSiD_3$ taken from the literature are added for reference (see text for details). The range of experimental C_Q-values is shown as a grey bar.

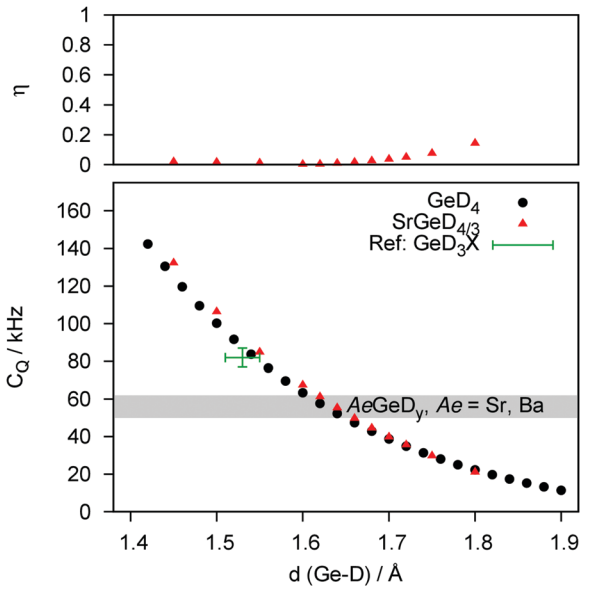

Fig. 4 DFT derived distance dependence C_Q and the corresponding asymmetry parameter η of GeD_4, and $SrGeD_{4/3}$. Experimental data of germane derivatives GeD_3X (X = D, CH_3) taken from the literature are added for reference (see text for details). The range of experimental C_Q-values is shown as a grey bar.

4 Discussion

This work takes advantage of NMR spectroscopy and DFT calculations to improve the precision of diffraction derived data. The local approach aims to overcome limitations of the structurally averaging character of powder diffraction and to create a comprehensive understanding of the materials under investigation. We mainly focus on the relation between quadrupolar coupling strengths and the corresponding bond lengths. We further discuss other NMR features such as linewidths and isotropic shifts.

We use three independent approaches:

(i) an experimental determination of C_Q values

(ii) a theoretical calculation of C_Q values based on DFT optimised models. They are based on the crystallographic models without non-stoichiometry effects.

(iii) a DFT-modelling approach towards an element–deuterium distance dependency which is verified against an independent model system, *i.e.*, DFT calculations of the molecular TtD_4 compounds.

The synthesis of these approaches allows us to recalculate bond lengths from experimental C_Q values.

4.1 Quadrupole interactions

Quadrupole interactions of those ^{2}H nuclei that bind to *Tt* atoms were measured in terms of C_Q in all samples. The results agree well with those values obtained from DFT optimized structures (Table 1). It is important to point out again, that diffraction based structural models suffer from large estimated uncertainties. Therefore, the precision of the actual bond lengths is not very high. This underlines the importance of combining different methods, experiment and modelling, to improve the structural and especially the bonding picture we have of these compounds.

In a first step, we can consider some general trends comparing calculated NMR parameters from the DFT optimised structure and experimental ones. The only mismatch between calculated and measured C_Q occurs for the second chain site in $SrGeD_{4/3-x}$ and $BaGeD_{5/3-x}$. DFT clearly underestimates the quadrupolar coupling strength, which indicates that the bond length is even shorter than expected from DFT calculations. According to DFT, the uncertainty must be assigned to the single-chain polyanions as depicted in Fig. 5. From the sole experimental (NMR) point of view, it is not possible to differentiate between these two main chain sites.

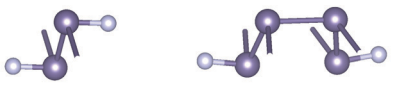

		D1	D2	D4	D3
$SrSiD_{5/3}$:	$C_{Q,DFT}$ =	63.3	63.7	57.3	58.0
	η_{DFT} =	0.11	0.09	0.02	0.01
$BaGeD_{5/3}$:	$C_{Q,DFT}$ =	55.3	55.7	49.8	50.3
	η_{DFT} =	0.05	0.03	0.02	0.02

Fig. 5 Single-chain (left) and double-chain polyanions (right) of $AeTtD_{5/3-x}$. There are four crystallographically independent deuterium sites (D1 to D4). Due to molecular pseudo-symmetry NMR parameters only deviate for the different polyanions. Large grey spheres are Si or Ge; small white spheres are D.

In a second step, the experimental quadrupole splittings will be assigned to discrete bond length values by DFT modelling. The quadrupole coupling of D is a most sensitive tool to probe electronic properties of a nucleus' closest environment. DFT confirms that for different *Tt* elements the interatomic distance to D changes systematically. And since these bond lengths or even the binding character are still a subject of controversy as mentioned in the beginning of this paper, we calculated a general distance dependence of C_Q for Si (Fig. 3) and Ge (Fig. 4) as bonding partners (Sn as bonding partner is given in the ESI,† Fig. S4). We propose, that the observed trend is independent of the model system. This is underlined by the fact, that the curves determined for a molecular system (TtD_4) and for the Zintl phase deuterides behave quantitatively equal.

The DFT-derived curves can be used to calculate values for *Tt*–D bond lengths from experimental quadrupole splittings (see ESI,† Fig. S2–S4; Tables S1 and S2). The distance dependency can be verified against literature values at first. For a couple of silane derivatives, SiD_3X quadrupole coupling constants were determined.[45–47] We can use them to calculate bond lengths of 1.49(1) Å (X = D), 1.50(1) Å (X = CH_3) and 1.50(1) Å (X = C_6H_5). Typical Si–D bond lengths in molecular compounds are 1.47–1.49 Å as determined for disilane.[48,49] For the Zintl-like deuteride β-$KSiD_3$, which exhibits monomeric SiD_3^--moieties, bond lengths (1.537(8) and 1.545(6) Å at 4 K[50]) and the quadrupole splitting (C_Q = 72.0(5) kHz at 200 K[51]) are known. From our curves we can estimate the bond length as 1.55(1) Å which fits the literature value. For germane[52] and methylgermane[53] the bond lengths can be estimated as 1.55(2) Å which is a typical value, *i.e.* 1.517 Å (GeD_4 at 4 K[54]) to 1.541 Å (Ge_2H_6[55]). For stannane[56] the bond length can be estimated as 1.72(2) Å which fit the neutron diffraction derived bond length of 1.706(3) Å.[54] From our experimental C_Q values we can evaluate the following bond lengths:

$CaSiD_{4/3-x}$	1.56(1) Å
$SrSiD_{5/3-x}$	1.58(1) Å (single chain polyanion)
	1.53(1) Å (double chain polyanion)
$BaSiD_{2-x}$	1.59(1) Å
$SrGeD_{4/3-x}$	1.65(1) Å
$BaGeD_{5/3-x}$	1.65(1) Å (single chain polyanion)
	1.61(1) Å (double chain polyanion)
$BaSnD_{4/3-x}$	1.84(1) Å

Single and double chain polyanions are assigned according to the trend derived from DFT structures (*cf.* Fig. 5). A comparison to diffraction- and DFT-derived bond lengths is given in Table 2.

4.2 Linewidths

DFT calculations and NMR offer further insight into the nature of the narrow lines shown in Fig. 2. The linewidth in particular tells us a lot about the void's geometry in which the nuclei are placed. First, even though we are investigating powdered samples, broadening effects due to shift anisotropy in ^{1}H and ^{2}H are known to be

Table 2 Comparison of Tt–D (Tt = Si, Ge, Sn) bond lengths as determined by Rietveld refinement using neutron powder diffraction data (NPD), optimized by density functional theory (DFT), and calculated from experimental C_Q values (NMR)

Compound		NPD $d(Tt$–D)/Å	DFT $d(Tt$–D)/Å	NMR $d(Tt$–D)/Å
$BaSiD_{2-x}$		1.641(5)[22]	1.573[22]	1.59(1)
$SrSiD_{5/3-x}$	(D1)	1.43(4)[23,24]	1.576[23,24]	1.53(1)
	(D2)	1.58(4)[23,24]	1.576[23,24]	
	(D3)	1.82(4)[23,24]	1.601[23,24]	1.58(1)
	(D4)	1.50(4)[23,24]	1.599[23,24]	
$CaSiD_{4/3-x}$		1.84[21]	1.58[20]	1.56(1)
$SrGeD_{4/3-x}$		1.521(9)[22]	1.667[22]	1.65(1)
$BaGeD_{5/3-x}$	(D1)	1.61(5)[23,24]	1.638[23,24]	1.61(1)
	(D2)	1.75(5)[23,24]	1.639[23,24]	
	(D3)	1.57(5)[23,24]	1.663[23,24]	1.65(1)
	(D4)	1.55(6)[23,24]	1.662[23,24]	
$BaGeD_{4/3-x}$		1.858(8)[22]	1.867[22]	1.84(1)

small because of the low number of electrons and can therefore be neglected.

Second, the samples under investigation not only show comparatively large widths, we also notice rather significant differences when comparing different samples (Fig. 2). Especially under fast spinning MAS (Fig. 6), the remaining widths vary substantially, sometimes being apparently structured like several lines in superposition. This implies that the *Ae* environment is slightly variable. Being essentially independent of the external magnetic field (data not shown) further indicates the broadening must stem from dipolar or quadrupolar interactions.

Magnetic dipole interaction can easily be calculated using the method of moments.[25,57] The coupling is chiefly homonuclear, *i.e.* ^{2}H will interact with other ^{2}H in its vicinity, because other NMR active nuclei in our systems have a low abundance. We receive consistently a broadening from magnetic dipole interactions of about 1–1.5 kHz for each sample.

In $BaSiD_{2-x}$, the linewidth is only 1.5(1) kHz, in agreement with the calculated dipole–dipole coupling. This is confirmed by diffraction and DFT calculations where only a single, highly symmetric crystallographic site is found for the *Ae* voids.

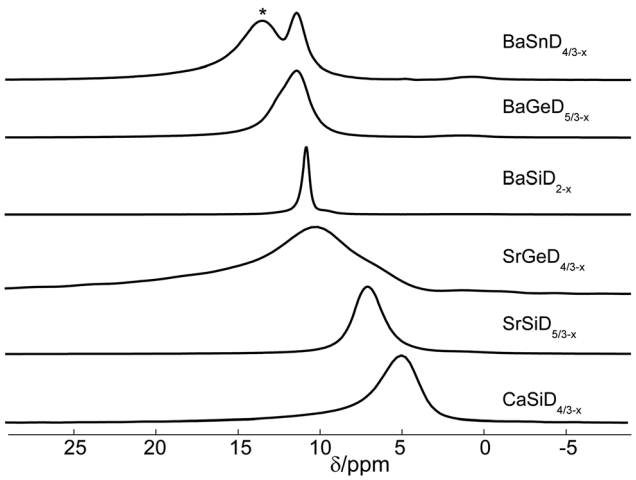

Fig. 6 Isotropic region of the ^{2}H MAS spectra. The asterisk indicates signal from a side product.

For the other samples, static NMR linewidths are much broader, up to 6–7 kHz. Dipolar coupling is not strong enough to account for such a broadening. However, the crystallographic models show three ($CaSiD_{4/3}$ structure type) to six ($SrSiD_{5/3}$ structure type) distinct crystallographic sites. The corresponding tetrahedra deviate from their equilateral shape leaving a slightly non-cubic environment to the ^{2}H nuclei in their middle with non-vanishing EFGs, yielding small quadrupolar splittings.

These quadrupole couplings cannot be resolved experimentally, because the present broadening from dipole interactions and additional effects smooth out individual features. DFT calculates C_Q values between 0.31 and 8.36 kHz. The interactions' symmetry (η) further varies between 0.03 and 0.86. Thus, in all samples except for $BaSiD_{2-x}$, DFT reveals that the narrow lines are composed of three to six components differing in C_Q and η. The combined effects, including magnetic dipole broadening and a small contribution from shift anisotropies, will then result in a NMR line broadening of several kHz. Possible differences in isotropic shift will also contribute to the linewidth. In Table 1 we give for each sample with multiple *Ae* sites the range of the calculated C_Q values and compare them to the linewidths (Λ) obtained by static FID measurements.

4.3 Shifts

Though the total range of ^{2}H shifts is rather small, significant differences in the sample series can be identified. The isotropic lines under MAS of the six samples are given in Fig. 6. For $BaSnD_{4/3-x}$ an additional signal is present around 13 ppm. It seems to be stemming from a side product as its shift together with the fact that intense spinning sidebands indicating a large quadrupolar splitting are present that don't go along with the identification of a deuteride in a tetrahedral void. Maybe the signal is due to decomposition within the MAS rotor.

Because of the large frequency distribution for the spinning sidebands of the quadrupolar lineshape, their central line is barely visible in comparison to the narrow line. As can be seen in Table 1, there are some small variations for the isotropic shifts of chain sites across the samples which will not be discussed further. Bonding partner and bond length are expected to have an influence on the chemical shift.

More interestingly, the isotropic shifts of the narrow lines seem to be a function of the surrounding atoms. Going from calcium to strontium and barium, an increase in isotropic shift is observed. A similar observation was found for CaH_2, SrH_2 and BaH_2[58] where the ^{1}H shift was investigated by line narrowing techniques on static samples. Here, it was concluded that the shift correlates with the electronegativity of the alkaline-earth element. Our investigations of SrD_2 and BaD_2 yielded isotropic shifts of 5.6 and 10.5 ppm, respectively (data not shown). Though there is only a limited number of samples, there seems to be a systematic effect. The large linewidth of $SrGeD_{4/3-x}$ prevents a more accurate assignment and the shift given in Table 1 represents only that of the maximum intensity. Whereas calculations of quadrupolar interactions are typically quite reliable, calculation of chemical shifts is more demanding especially for small shift ranges. In the future, these calculations might be useful to give a more detailed picture on expected isotropic shifts.

5 Conclusions

We combine NMR and DFT techniques to further improve the understanding of structural and bonding properties of the homologue series of Zintl phase deuterides $AeTtD_{(1+y)}$, *Ae* = Ca–Ba, *Tt* = Si–Sn, $y \approx 1/3$, 2/3 or 1. NMR is well suited to study Zintl phase deuterides since it allows to distinguish and characterize the individual features of the ionic (D^-) and the covalent deuterium-bound polyanionic moieties.

We further derived a generalized deuterium-element bond length dependency of the ^{2}H quadrupole interaction. Typically, the determination of hydrogen/deuterium positions can only be done reliably from neutron diffraction data. Complex crystal structures or poorly crystalline samples can complicate the crystallographic approach as was the case for the $AeTtD_{(1+y)}$ family.

NMR measurements allow a comparatively fast and highly efficient lab-based approach to evaluate covalent element–deuterium bond length. Preparation, optimization and measurements can be done within hours. This approach can thus be used, *e.g.* to assign possible deuterium sites in a crystallographic model from X-ray data that are insensitive to hydrogen/deuterium. It might be even suitable to determine *X*–D bond lengths (*X* = Si, Ge, Sn) reliably without crystallographic model. The evaluation of quadrupolar interactions thus expands the toolbox of NMR crystallography. It allowed us to refine *Tt*–D covalent bond lengths of Zintl phase deuterides which were only described with low precision by diffraction models so far. To verify this general approach, further studies on similar systems would be beneficial.

Furthermore, DFT calculations confirm the presence of small and distributed quadrupole interactions for those ^{2}H nuclei occupying the *Ae* void sites. Together with experimental evidence from static and MAS NMR, the findings provide a comprehensive local chemical picture of the present materials. The isotropic chemical shifts of the hydridic signals, even though rather broad due to the scattered crystal sites, indicate an increasing shift with larger surrounding atom.

Conflicts of interest

There are no conflicts to declare.

Acknowledgements

R. G. acknowledges the funding by the MacDiarmid Institute and Leipzig University. R. G. and M. B. acknowledge the help of M. Lindel. H. K. and H. A. thank the Deutsche Forschungsgemeinschaft (DFG, grant Ko1803/8-1) and the Fonds der Chemischen Industrie (Grant 194371) for financial support.

Notes and references

1 E. Zintl, *Angew. Chem.*, 1939, **52**, 1–6.
2 R. Nesper, *Angew. Chem.*, 1991, **103**, 805–834.
3 O. Janka and S. M. Kauzlarich, *Zintl Compounds*, John Wiley & Sons, Ltd, 2011.
4 R. Nesper, *Z. Anorg. Allg. Chem.*, 2014, **640**, 2639–2648.
5 U. Häussermann, V. F. Kranak and K. Puhakainen, *Struct. Bonding*, 2010, **139**, 143–161.
6 F. Gingl, T. Vogt and E. Akiba, *J. Alloys Compd.*, 2000, **306**, 127–132.
7 T. Björling, D. Noréus and U. Häussermann, *J. Am. Chem. Soc.*, 2006, **128**, 817–824.
8 M. H. Lee, T. Björling, B. C. Hauback, T. Utsumi, D. Moser, D. Bull, D. Noréus, O. F. Sankey and U. Häussermann, *Phys. Rev. B: Condens. Matter Mater. Phys.*, 2008, **78**, 195209.
9 M. J. Evans, G. P. Holland, F. J. Garcia-Garcia and U. Häussermann, *J. Am. Chem. Soc.*, 2008, **130**, 12139–12147.
10 V. F. Kranak, M. J. Evans, L. L. Daemen, T. Proffen, M. H. Lee, O. F. Sankey and U. Häussermann, *Solid State Sci.*, 2009, **11**, 1847–1853.
11 M. J. Evans, V. F. Kranak, F. J. Garcia-Garcia, G. P. Holland, L. L. Daemen, T. Proffen, M. H. Lee, O. F. Sankey and U. Häussermann, *Inorg. Chem.*, 2009, **48**, 5602–5604.
12 M. H. Lee, M. J. Evans, L. L. Daemen, O. F. Sankey and U. Häussermann, *Inorg. Chem.*, 2008, **47**, 1496–1501.
13 M. J. Evans, M. H. Lee, G. P. Holland, L. L. Daemen, O. F. Sankey and U. Häussermann, *J. Solid State Chem.*, 2009, **182**, 2068–2073.
14 H. Fahlquist, D. Noréus, S. Callear, W. I. F. David and B. C. Hauback, *J. Am. Chem. Soc.*, 2011, **133**, 14574–14577.
15 H. Fahlquist, D. Noréus and M. H. Sørby, *Inorg. Chem.*, 2013, **52**, 4771–4773.
16 H. Fahlquist and D. Noréus, *Inorg. Chem.*, 2013, **52**, 7125–7129.
17 J. Ångström, R. Johansson, T. Sarkar, M. H. Sørby, C. Zlotea, M. S. Andersson, P. Nordblad, R. H. Scheicher, U. Häussermann and M. Sahlberg, *Inorg. Chem.*, 2016, **55**, 345–352.
18 R. Nedumkandathil, V. F. Kranak, R. Johansson, J. Ångström, O. Balmes, M. S. Andersson, P. Nordblad, R. H. Scheicher, M. Sahlberg and U. Häussermann, *J. Solid State Chem.*, 2016, **239**, 184–191.
19 H. Auer, R. Nedumkandathil, U. Häussermann and H. Kohlmann, *Z. Anorg. Allg. Chem.*, 2019, **645**, 175–181.
20 N. Ohba, M. Aoki, T. Noritake, K. Miwa and S.-I. Towata, *Phys. Rev. B: Condens. Matter Mater. Phys.*, 2005, **72**, 075104.
21 H. Wu, W. Zhou, T. J. Udovic, J. J. Rush and T. Yildirim, *Phys. Rev. B: Condens. Matter Mater. Phys.*, 2006, **74**, 224101.
22 H. Auer, R. Guehne, M. Bertmer, S. Weber, P. Wenderoth, T. C. Hansen, J. Haase and H. Kohlmann, *Inorg. Chem.*, 2017, **56**, 1061–1071.
23 H. Auer, R. Schlegel, O. Oeckler and H. Kohlmann, *Angew. Chem., Int. Ed.*, 2017, **56**, 12344–12347.
24 H. Auer, R. Schlegel, O. Oeckler and H. Kohlmann, *Angew. Chem.*, 2017, **129**, 12515–12518.
25 A. Abragam, *The Principles of Nuclear Magnetism*, Oxford University Press, 1983.
26 M. Aoki, N. Ohba, T. Noritake and S. Towata, *Appl. Phys. Lett.*, 2004, **85**, 387–388.
27 M. Armbruster, M. Wörle, F. Krumeich and R. Nesper, *Z. Anorg. Allg. Chem.*, 2009, **635**, 1758–1766.
28 E. L. Hahn, *Phys. Rev.*, 1950, **80**, 580.
29 J. Powles and P. Mansfield, *Phys. Lett.*, 1962, **2**, 58–59.

30 D. Massiot, F. Fayon, M. Capron, I. King, S. L. Calvé, B. Alonso, J.-O. Durand, B. Bujoli, Z. Gan and G. Hoatson, *Magn. Reson. Chem.*, 2002, **40**, 70–76.
31 X. Gonze, J.-M. Beuken, R. Caracas, F. Detraux, M. Fuchs, G.-M. Rignanese, L. Sindic, M. Verstraete, G. Zerah, F. Jollet, M. Torrent, A. Roy, M. Mikami, P. Ghosez, J.-Y. Raty and D. Allan, *Comput. Mater. Sci.*, 2002, **25**, 478–492.
32 X. Gonze, *Z. Kristallogr.*, 2005, **220**, 558–562.
33 X. Gonze, B. Amadon, P.-M. Anglade, J.-M. Beuken, F. Bottin, P. Boulanger, F. Bruneval, D. Caliste, R. Caracas, M. Côté, T. Deutsch, L. Genovese, P. Ghosez, M. Giantomassi, S. Goedecker, D. Hamann, P. Hermet, F. Jollet, G. Jomard, S. Leroux, M. Mancini, S. Mazevet, M. Oliveira, G. Onida, Y. Pouillon, T. Rangel, G.-M. Rignanese, D. Sangalli, R. Shaltaf, M. Torrent, M. Verstraete, G. Zerah and J. Zwanziger, *Comput. Phys. Commun.*, 2009, **180**, 2582–2615.
34 X. Gonze, F. Jollet, F. A. Araujo, D. Adams, B. Amadon, T. Applencourt, C. Audouze, J.-M. Beuken, J. Bieder, A. Bokhanchuk, E. Bousquet, F. Bruneval, D. Caliste, M. Côté, F. Dahm, F. D. Pieve, M. Delaveau, M. D. Gennaro, B. Dorado, C. Espejo, G. Geneste, L. Genovese, A. Gerossier, M. Giantomassi, Y. Gillet, D. Hamann, L. He, G. Jomard, J. L. Janssen, S. L. Roux, A. Levitt, A. Lherbier, F. Liu, I. Lukačević, A. Martin, C. Martins, M. Oliveira, S. Poncé, Y. Pouillon, T. Rangel, G.-M. Rignanese, A. Romero, B. Rousseau, O. Rubel, A. Shukri, M. Stankovski, M. Torrent, M. V. Setten, B. V. Troeye, M. Verstraete, D. Waroquiers, J. Wiktor, B. Xu, A. Zhou and J. Zwanziger, *Comput. Phys. Commun.*, 2016, **205**, 106–131.
35 http://www.abinit.org, Abinit v. 8.2.2, GNU General Public License.
36 J. P. Perdew, K. Burke and M. Ernzerhof, *Phys. Rev. Lett.*, 1996, **77**, 3865–3868.
37 M. A. Marques, M. J. Oliveira and T. Burnus, *Comput. Phys. Commun.*, 2012, **183**, 2272–2281.
38 P. E. Blöchl, *Phys. Rev. B: Condens. Matter Mater. Phys.*, 1994, **50**, 17953–17979.
39 M. Torrent, F. Jollet, F. Bottin, G. Zérah and X. Gonze, *Comput. Mater. Sci.*, 2008, **42**, 337–351.
40 https://www.abinit.org/downloads/PAW2, JTH PAW atomic datasets, version 1.0.
41 F. Jollet, M. Torrent and N. Holzwarth, *Comput. Phys. Commun.*, 2014, **185**, 1246–1254.
42 H. J. Monkhorst and J. D. Pack, *Phys. Rev. B: Solid State*, 1976, **13**, 5188–5192.
43 D. M. Bishop and L. M. Cheung, *Phys. Rev. A: At., Mol., Opt. Phys.*, 1979, **20**, 381–384.
44 N. Stone, *At. Data Nucl. Data Tables*, 2005, **90**, 75–176.
45 U. Lähteenmäki, L. Niemelä and P. Pyykkö, *Phys. Lett. A*, 1967, **25**, 460–461.
46 R. Ader and A. Loewenstein, *Mol. Phys.*, 1974, **27**, 1113–1116.
47 B.-M. Fung and I. Y. Wei, *J. Am. Chem. Soc.*, 1970, **92**, 1497–1501.
48 L. O. Brockway and J. Y. Beach, *J. Am. Chem. Soc.*, 1938, **60**, 1836–1846.
49 B. Beagley, A. Conrad, J. Freeman, J. Monaghan, B. Norton and G. Holywell, *J. Mol. Struct.*, 1972, **11**, 371–380.
50 W. S. Tang, J.-N. Chotard, P. Raybaud and R. Janot, *J. Phys. Chem. C*, 2014, **118**, 3409–3419.
51 R. Nedumkandathil, A. Jaworski, A. Fischer, C. Österberg, Y.-C. Lin, M. Karlsson, J. Grins, A. J. Pell, M. Edén and U. Häussermann, *J. Phys. Chem. C*, 2017, **121**, 5241–5252.
52 V. Hovi, U. Lähteenmäki and R. Tuulensuu, *Phys. Lett. A*, 1969, **29**, 520–521.
53 R. Ader and A. Loewenstein, *J. Am. Chem. Soc.*, 1974, **96**, 5336–5340.
54 I. J. Maley, D. H. Brown, R. M. Ibberson and C. R. Pulham, *Acta Crystallogr., Sect. B: Struct. Sci.*, 2008, **64**, 312–317.
55 B. Beagley and J. J. Monaghan, *Trans. Faraday Soc.*, 1970, **66**, 2745.
56 L. Niemela and J. Mäkelä, *Phys. Lett. A*, 1973, **43**, 343–344.
57 J. V. Vleck, *Phys. Rev.*, 1948, 116–183.
58 A. T. Nicol and R. W. Vaughan, *J. Chem. Phys.*, 1978, **69**, 5211–5213.